Proceedings of
11th European Conference on Turbomachinery Fluid dynamics & Thermodynamics
ETC11, March 23-27, 2015, Madrid, Spain

TOWARD A HIGH-ORDER PRESERVING SLIDING-MESH APPROACH FOR COMPUTATIONAL AEROACOUSTICS IN SUBSONIC TURBOMACHINERY

C. Foulquié [1], *S.Khelladi* [1], *L. Ramirez* [2], *X. Nogueira* [2], *M. Deligant* [1], *J. Mardjono* [3], *M. Henner* [4]

[1] Laboratoire de Dynamique des Fluides, Arts et Métiers PariTech,
(151 boulevard de l'Hôpital, 75013 Paris, France)
[2] Grupo de Métodos Numéricos en Ingeniería,
(GMNI, Universidade da Coruña , A Coruña, Spain)
[3] Acoustics Department, Safran-Snecma,
(Rond-point René Ravaud, 77550 Réau, France)
[4] Fan system simulation department, Valeo engine cooling,
(8 rue Louis Lormand, 78320 La Verrière, France)
Contact charles.foulquie@ensam.eu

ABSTRACT

The aeroacoustic analogy is the hybrid technique most used to predict acoustic noise of open rotor turbo-machines. However it is not appropriate to turbo-machines operating in confined spaces - where the diffractions, reflections and near-field flow effects can not be neglected. To overcome this issue, acoustic sources are propagated using linearized Euler equation and rotor motion is taken into account by using a *sliding mesh* method. This technique allows relative sliding of one grid adjacent to another grid. In addition, we propose a high-order finite volume solver (based on Moving Least Squares approximation MLS), which works on unstructured grid, in order to address most of the industrial applications and their complex geometries. In this paper, two families of MLS-based sliding mesh method are presented. A comparison between the accuracy of the different sliding mesh approaches is made by using a theoretical acoustic benchmark.

NOMENCLATURE

ρ_0	Mean flow density.	$\boldsymbol{V_0}$	Mean flow velocity.
u_0	Axial mean flow velocity.	$\boldsymbol{V_{rel}}$	Grid velocity
u_{rel}	Axial grid velocity.	T_m	Medium cell size.
v_0	Average value of transversal flow velocity.	$\boldsymbol{x_I}$	Position vector of the I centroid.
v_{rel}	Transversal grid velocity.	$\Omega_{\boldsymbol{x}_I}$	Vicinity of $\boldsymbol{x}_I$.
p_0	Mean flow pressure.	$\mathcal{S}(I)$	Neighborhood (or Stencil) of $\boldsymbol{x}_I$.
$\boldsymbol{U}$	Conservative variable vector.	$u(\boldsymbol{x})$	Conservative variable.
$\delta\rho$	Flow density fluctuation.	$\hat{u}(\boldsymbol{x})\|_I$	Approximation of u in the vanicity of $\boldsymbol{x_I}$.
δu	Axial flow velocity fluctuation.	J	The Cells inside the stencil centered on $\boldsymbol{x_I}$.
δv	Transversal flow velocity fluctuation.	u_J	Conservative variable vector at the J centroid.
δp	Flow pressure fluctuation.	$N^J_{[\boldsymbol{x}_I]}(\boldsymbol{x})$	Shape function of the J centroid centered on $\boldsymbol{x_I}$.
γ	Adiabatic index.	n_{min}	Minimum number of point in the stencil.
I	Cell Identifier.	p	Additional point in the stencil.
A_I	Area of the I cell.	n_t	Total number of point in the stencil.
L_I	Contour length of the I cell.	W_e^2, W_e^1	2D and 1D exponential weight function.
$\mathbb{F}$	Vector of flux.	x_I	Axial coordinate of the I cell.
n_P	Normal vector of the edge at point P.	y_J	Transversal coordinate of the J cell.

$\boldsymbol{x}_J$	Position vector of the J centroid.	N_c	Total number of cell in the domain.
x_J, y_J	coordinates of the J cell.	$\epsilon_{P,I}$	Difference between p_I^{num} and p_I^{ex}
d_m	Smoothing length	p_I^{ex}	Exact pressure at the I centroid.
$\boldsymbol{\kappa}$	Shape parameters vector.	p_I^{num}	Numerical pressure at the I centroid.
κ_x, κ_y	Axial and Transversal shape parameter.	A	Area of the domain.
	Transversal shape parameter.	μ_{IJ}	Pseudo mass matrix element's.
x_S, y_S	Axial and Transversal coordinate	$\mathbb{M}$	Pseudo mass matrix.
	of the source.	$\boldsymbol{R}$,$\boldsymbol{u}$	Space residual vector of the
x_R, y_R	Axial and Transversal coordinate		one-variable system and vector of
	of the moving grid center.		one-variable values at centroids.
d_1, d_2	Fixed grid and moving grid diameter.	u_I	Value of a variable at the I centroid.
$\boldsymbol{U}_P^{(R)}, \boldsymbol{U}_P^{(L)}$	Extrapolated left and right variables vector.	ω	Adimensional rotational velocity.
$\boldsymbol{e}_k$, λ_k	Eigenvectors and eigenvalues	$\hat{\boldsymbol{F}}$	Approximate Riemann Solver.
	of the Roe matrix	u_s	Axial mean shear flow velocity
α_k	Wave at inter cell boundary	M_s	Maximum Mach number
c_∞,ρ_∞,$1/\gamma_\infty$	Velocity, density and pressure scale	r	Radial distance to the Domain center
ω_n	Angular frequency of Monopole source	$L_2(p)$	Quadratic mean errors of pressure
ϵ	Amplitude of monopole source	$L_\infty(p)$	Maximum error of pressure

INTRODUCTION

In Aeroacoustics, two computational approaches are possible: the direct and the hybrid approach. Currently, the most used approach is the hybrid method, especially in the presence of complex geometries (rotor/stator interactions, fans and etc.). It consists of separating the aerodynamic contribution from the acoustic one. Thus, the computational constraints and time are considerably reduced. This is the approach adopted in this work. The aeroacoustic analogy is the hybrid technique most used to predict the acoustic noise of open rotor turbo-machines. However, it is not appropriate to turbo-machines operating in confined spaces - where the diffractions, reflections and near-field flow effects can not be neglected. To overcome this issue, acoustic sources are propagated using Linearized Euler Equation (LEE) . In addition to the use of LEE, the main issue in this work is to consider the rotor motion into the propagation field. One of the numerical technique widely used is the sliding mesh method.

This technique allows relative sliding from one grid adjacent to another grid. In the case of turbomachinery, one of the grids is related to the stator (fixed) and the other is related to the rotor (moving). Therefore, non-matching cells may appear at the interface between static and moving grids. As shown in Fig. 1, this situation introduces a problem of interpolation. In addition to that, when a high-order method is applied, the interpolation scheme used in the sliding mesh model needs to present at least the same order of convergence than the numerical scheme, in order to prevent loss of accuracy.

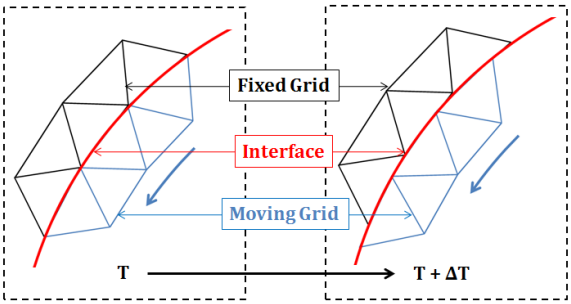

Illustration of the sliding mesh concept.
The moving grid slide over the fixed grid

A high order ($\geqslant 3$) discontinuous Galerkin method with sliding mesh capabilities was proposed by Ferrer and Willden [2012]. In this work, it is presented a sliding mesh model based on the use of

Moving Least Squares (MLS) approximants. A high-order finite volume method is applied and it computes the derivatives of the Taylor's expansion in each control volume using MLS approximants. In addition, this new sliding mesh model fits naturally in a high-order finite volume framework for the computation of acoustic wave propagation into turbomachinery. Using a numerical benchmark test, four different approaches for the transmission of information from one grid to another will be studied.

1 NUMERICAL METHODS

1.1 General framework:

Governing equations: We consider the behaviour of small acoustic perturbations $\boldsymbol{U} = [\delta\rho, \rho_0\delta u, \rho_0 \delta v, \delta p]^T$ on top of a steady mean flow $\boldsymbol{U_0} = [\rho_0, u_0, v_0, p_0]^T$ by using Linearized Euler Equation LEE. To achieve numerical stability, the equations are written in a conservative form, as following:

$$\frac{\partial \boldsymbol{U}}{\partial t} + \frac{\partial \boldsymbol{E}}{\partial x} + \frac{\partial \boldsymbol{F}}{\partial y} + \boldsymbol{H} = \boldsymbol{S} \tag{1}$$

where $\boldsymbol{E}$ and $\boldsymbol{F}$ are the flux vectors. $\boldsymbol{S}$ represents a possible source term. The vector $\boldsymbol{H}$ contains the refraction terms (It is equal to zero if the mean flow is uniform). Complete expressions of the vectors are given in Appendix 1. To take into account the motion of the grid we write the governing equation in an Arbitrary Lagrangian Eulerian (ALE) setting. In other words, we substract the grid velocity $\boldsymbol{V_{rel}} = [u_{rel}, v_{rel}]^T$ from mean flow velocity $\boldsymbol{V_0} = [u_0, v_0]^T$. The cases $\boldsymbol{V_{rel}} = \boldsymbol{V_0}$ corresponds to a Lagrangian system, and $\boldsymbol{V_{rel}} = \boldsymbol{0}$ is a Eulerian one. In the present formulation, $\boldsymbol{V_{rel}}$ is arbitrarily specified.

Spatial discretization approach: To discretize this problem we use a cell-centered finite volume (FV) method on triangular unstructured grid. Let's consider $\mathbb{F}= (\boldsymbol{E}, \boldsymbol{F})^T$. The integration of Eqn. (1) into a control surface A_I gives:

$$\underbrace{\frac{1}{A_I}\int_{A_I} \frac{\partial \boldsymbol{U}}{\partial t}\,\mathrm{d}s}_{A} = \underbrace{-\frac{1}{A_I}\int_{A_I} \boldsymbol{\nabla}\cdot\mathbb{F}\,\mathrm{d}s}_{B} + \underbrace{\frac{1}{A_I}\int_{A_I} (\boldsymbol{S}-\boldsymbol{H})\,\mathrm{d}s}_{C} \tag{2}$$

Convective flux approximation: The surface integration of convective flux (Eqn.(2)) is transformed by the use of divergence theorem to contour integration :

$$\int_{A_I} \boldsymbol{\nabla}\cdot\mathbb{F}\,\mathrm{d}s = \oint_{L_I} \mathbb{F}\cdot\boldsymbol{n}\,\mathrm{d}l \tag{3}$$

Therefore, the finite volume method lead us to a Riemann problem for convective flux estimation at each integration point of inter-cell boundary L_I. Let's consider P an integration point which belong to an inter-cell boundary. As it is shown in Fig. 1, the global approach for the evaluation of flux at the P-point is the following:

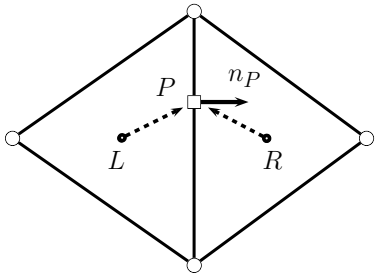

Fig. 1: Flux approximation at the P-point

– First, we extrapolate variables from the *left* centroid (L) and the *right* centroid (R) to the P-point by using a high order reconstruction which will be developed in the next section.

– Secondly, the extrapolated left $\boldsymbol{U}_P^{(L)}$ and right $\boldsymbol{U}_P^{(R)}$ states at the edge integration point are used as input data for an approximate Riemann solver : $\mathbb{F}(\boldsymbol{U}_P)\cdot\boldsymbol{n}_P \approx \hat{\boldsymbol{F}}(\boldsymbol{U}_P^{(L)}, \boldsymbol{U}_P^{(R)}, \boldsymbol{n}_P)$

Approximate Riemann solver in ALE setting: For the sake of accuracy, Roe's approximate Riemann solver has been selected among other (Rusanov, FVS, LLF ...) to carry out the numerical simulations using moving grids :

$$\hat{\boldsymbol{F}}(\boldsymbol{U}_P^{(L)}, \boldsymbol{U}_P^{(R)}, \boldsymbol{n}_P) = \frac{1}{2}\left[\mathbb{F}(\boldsymbol{U}_P^{(R)}) + \mathbb{F}(\boldsymbol{U}_P^{(L)})\right] \cdot \boldsymbol{n}_P - \frac{1}{2}\sum_{k=1}^{4} \tilde{\alpha_k}|\tilde{\lambda_k}|\tilde{e_k} \tag{4}$$

Where $\boldsymbol{e}_k$ and λ_k are respectively the eigenvector and the eigenvalues of the Roe's matrix. α_k represent the wave strengths along the eigenvector axes. It is remarkable that the eigenvalues of the Roe's matrix (which match to the wave speeds along eigenvector axes) "feel" the motion of the grid. In 2D the set of eigenvalues becomes $\tilde{\lambda_1}, \tilde{\lambda_2}, \tilde{\lambda_3}, \tilde{\lambda_4} = V_{0,n}^P - V_{rel,n}^P + c_0, x - V_{rel,n}^P - c_0, V_{0,n}^P - V_{rel,n}^P, V_{0,n}^P - V_{rel,n}^P$ where $V_{0,n}^P$ and $V_{rel,n}^P$ represent, respectively, the normal flow velocity and the normal grid velocity at cell interface boundary. The wave strengths and the eigenvectors remain unchanged with respect to a static mesh formulation. For more detail information about the Roe's in ALE setting please check on Trepanier et al. [1991] and Roe. [1981] publication.

1.2 High order reconstruction using MLS approximation

Estimation of high order derivatives of Taylor's expansion: The main difficulty in extrapolating variables from the centroid to the gauss node is estimating the higher order derivatives of Taylor's expansion. We overcome this difficulty by using the Moving Least Squares (MLS) approximation. For each cell (I), we start from a high-order representation of a variable $u(\boldsymbol{x})$ in the vicinity of $\boldsymbol{x_I}$, given by:

$$\hat{u}(\boldsymbol{x})|_I = \sum_{J \in \mathcal{S}(I)} N^J_{[\boldsymbol{x_I}]}(\boldsymbol{x}) \cdot u_J \tag{5}$$

where $\mathcal{S}(I) = \{J \in \mathbb{N},\ \boldsymbol{x_J} \in \Omega_{\boldsymbol{x}_I}\}$ is the stencil of the I cell (composed by the I cell and its neighborhood, see Fig. 2), $N^J_{[\boldsymbol{x}_I]}(\boldsymbol{x})$ is the shape function associated to the J cell obtained by using a weighted least-squares fitting procedure centred on $\boldsymbol{x_I}$. And u_J is the variable at the centroid of the J cell. Then, we use this representation of the solution to compute higher order derivatives. The shape functions are related to the grid topology. For a non-deforming grid, the shape function and its derivatives are calculated just once at the beginning of computation. We refer the intersted reader to Liu et al. [1997] and Cueto-Felgueroso et al. [2006, 2007].

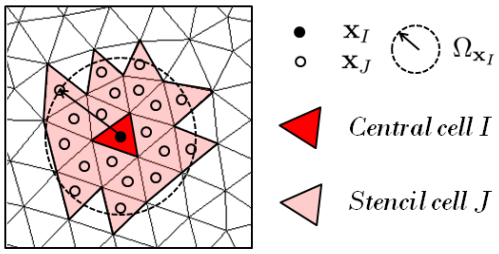

Fig. 2: MLS 5^{th} order scheme stencil (4^{th} order reconstruction) $n_{min} = 15$, $p = 4$

Stencil size: In this work, we use an uniform stencil size: $\forall i, \mathrm{card}(\mathcal{S}(I)) = n_t$. The minimum number of points in the stencil corresponds to the dimension of the polynomial basis used in the weighted least-squares fitting procedure. It is given by (in 2D) $n_{min} = (ord+1)(ord+2)/2$ where ord is the reconstruction order. If $n_t = n_{min}$, the FV-MLS scheme becomes unstable. To solve this problem, we introduce an additional number of points p such as $n_t = n_{min} + p$. It was observed that a p too large induces too much dissipation. This parameter depends on the reconstruction order and the quality of the grid.

Weight function: In order to ponderate the values of each centroid inside the stencil, a weight function is required. Here, we use the 1D-exponential weight function W^1_{exp} represented by Fig. 3, which is well suited for LEE and unstructured grids:

$$W(x_J - x_I, \kappa_x) = \frac{e^{-\left(\frac{s}{c}\right)^2} - e^{-\left(\frac{dm}{c}\right)^2}}{1 - e^{-\left(\frac{dm}{c}\right)^2}} \qquad (6)$$

where $s = |x_J - x_I|$, $j = 1, \ldots, n_x$, $d_m = 2\max(|x_J - x_I|)$ and $c = \frac{d_m}{\kappa_x}$. x_I is the x-coordinate of the I-cell centroid, κ_x is a shape parameter and d_m is the smoothing length.We recommend a lecture of the book of Liu [2003] for more details. The 2D-exponential W^2_{exp} is obtained by multiplying two 1D-exponentials W^1_{exp}:

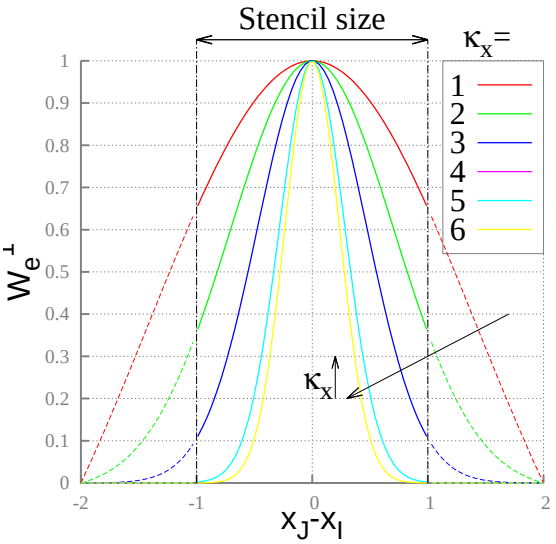

Fig. 3: Representation of the 1D-exponential weight function for different values of κ_x.

$$W^2_e(\boldsymbol{x_J} - \boldsymbol{x_I}, \boldsymbol{\kappa}) = W^1_e(x_J - x_I, \kappa_x) \cdot W^1_e(y_J - y_I, \kappa_y) \qquad (7)$$

The dispersion and dissipation characteristics of the FV-MLS method are strongly related to the choice of the shape parameters κ_x and κ_y. We refer the reader to Nogueira et al. [2010]. In the case of strongly directional node distribution the 1D-shape parameters could be different. In this work we use a faintly skewed unstructured grid, so: $\kappa_x = \kappa_y$.

Temporal term treatment: Using MLS approximants (Eqn. (5)), a development of time derivative integration (Part A of Eqn. (2)) for a conservative variable show us:

$$\int_{A_I} \left.\frac{\partial u}{\partial t}\right|_I ds = A_I \sum_{J \in \mathcal{S}(I)} \mu_{IJ} \frac{\partial u_J}{\partial t} \qquad (8)$$

where,

$$\mu_{IJ} = \frac{1}{A_I} \int_{A_I} N^J_{[\boldsymbol{x}_I]}(\boldsymbol{x}) ds \qquad (9)$$

So, the finite volume discretisation of 2D-LEE into a cell I gives:

$$\sum_{J \in \mathcal{S}(I)} \mu_{IJ} \frac{\partial u_J}{\partial t} = \underbrace{\bar{s}_I - \frac{1}{A_I} \sum_{i=1}^{3} \sum_{j=1}^{Ng} \boldsymbol{F}_{ij} \cdot \boldsymbol{n}_i w_{ij}}_{R(u_I)} \qquad (10)$$

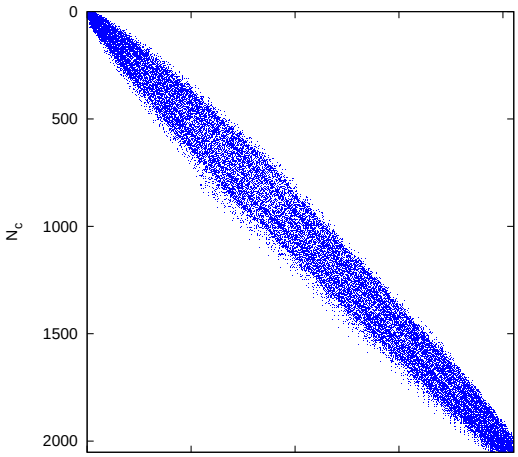

Fig. 4: Circular computational domain of $N_c = 2034$ cells without sliding mesh. The numerotation of cells start from the center of the grid with a distance criterium .

Finally, the general representation of the system to be solved for a variable u is:

$$\mathbb{M} \cdot \frac{\partial \boldsymbol{u}}{\partial t} = \boldsymbol{R} \qquad (11)$$

where $\mathbb{M} = \{\mu_{IJ}\}_{1 \leq (I,J) \leq N_c}$, $\boldsymbol{u} = [u_1, ..., u_{N_c}]^T$ and $\boldsymbol{R} = [R(u_1), ..., R(u_{N_c})]^T$. $\mathbb{M}$ is called pseudo mass matrix which expresses the relationship between the I cells and their nearest neighbors and $\boldsymbol{R}$ is the residual term vector. We can clearly see in Fig. 4 that $\mathbb{M}$ is a square matrix of size N_c.

1.3 MLS-based sliding mesh interface

The sliding takes place on a line that is called *interface*. Note that in practice, the interface is composed of two coincident edges. One of them belongs to the fixed grid and the other one to the moving mesh. As the moving grid slides over the fixed grid, the mesh is no longer conformal at the interface.

Transmission of information: We present two different approaches based on MLS approximation for the transmission of information from one grid to another. Let us consider a I cell on the interface:
Intersection approach: The flux at the interface edge of the I cell is split between the cell having an interface edge coincident. This procedure is illustrated in Fig. 5-A. The computation of the edge intersection introduces additional complexity in the coding as well as in the computing time.
Halo cell approach: Here, we create a halo-cell as a specular image of the I cell. This is schematically presented in Fig. 5-B. The MLS approximation in the vicinity of the halo cell (Eqn. (5)) is performed by using the stencil of the closest cell. But the computation of the shape function must be centered at the halo cell centroid. Then, the extrapolation of variables is done as usual using the new MLS approximation. However, this technique induces an error of mass conservation, but numerical experiments have shown that is of the same order than the variable error.

Stencil used at the interface: Two kind of stencil has been tested:
Full stencil: The total stencil of the I cell is computed at each time step by merging stencils of cell I and those cells having an interface edge coincident with cell I. As the stencil topology changes, the MLS shape functions and its derivatives must also be re-calculated at each time step. This procedure is performed on the interface cells and also on the cells near the interface. Finally, the full stencil formulation leads to a non-negligible additional computational cost. The final stencil of cell I is shown in Fig. 5-A and 5-B.
Half stencil: In order to avoid both the search of neighbors and the computation of the MLS shape functions at each time step, we suggest to employ a biased stencil, taking in account only cells from the grid in which the cell is placed (Fig. 5-A et 5-B). This half-stencil approach is expected to be less accurate than its full stencil counterpart because the computational stencil of cell I is not centred.

The ways to transfer information and compute the stencil at the interface leads us to four methods:

1-Full stencil intersections (FSI): Fig. 5-A.
2-Full stencil halo cell (FSH): Fig. 5-B.
3-Half stencil intersections (HSI): Fig. 5-A.
4-Half stencil halo cell (HSH): Fig. 5-B.

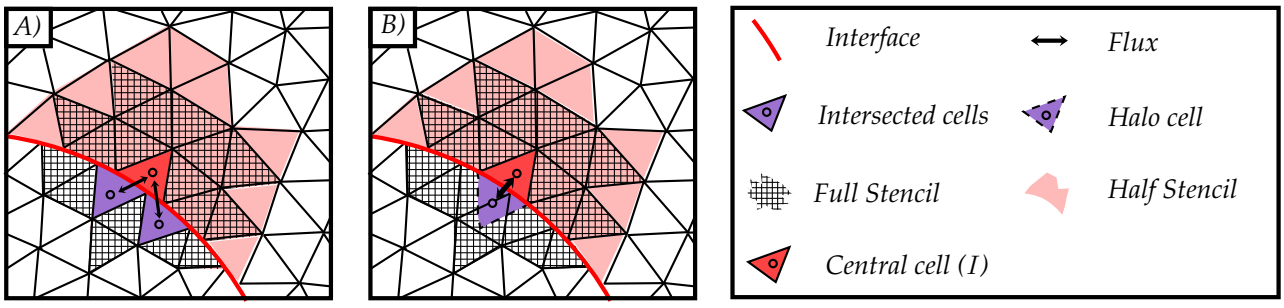

Figure 5: The four MLS-based sliding mesh interface approaches

2 NUMERICAL VALIDATION

2.1 Benchmark description

Acoustic pulse problem: The problem concerns the propagation of a Gaussian pulse using LEE. This is done for zero mean flow and constant mean density and pressure : $U_0 = [1, 0, 0, 1/\gamma]$. The source term, introduced in Eqn. 1 at $t = 0$, is:

$$\boldsymbol{S}(x, y) = \mathrm{e}^{-\frac{ln2}{b^2}r} \times [1\ 0\ 0\ 1]^T \tag{12}$$

where $r = [(x - x_s)^2 + (y - y_s)^2]^{1/2}$ is the radial distance to the domain's center. The half-width of the Gaussian pulse is set at $b = 3$. In what follows, all variables are nondimensionalized with the following reference scales: c_∞ for the velocity scale, ρ_∞ for the density scale, $1/\gamma_\infty$ for the pressure scale and T_m for the length scale where T_m is the medium cell size. The analytical solution of Gaussian pulse propagation can be easily calculated. Please see Bogey and Bailly [2002] and Tam and Webb [1993] for details.

Computational domain: According to Fig. 6, the computational domain is divided into two grids:

1. A circular fixed grid of diameter $d_1 = 100$ centred at $S(x_S = 0, y_S = 0)$.
2. A circular sliding grid of diameter $d_2 = 20$ centered at $R(x_R = 0, y_R = 20)$ which rotates around its center with a rotational velocity ω.

The source is located at $S(0, 0)$. In order to perform a non-axisymmetric benchmark, the moving grid is not centered on the source ($y_S \neq y_R$).

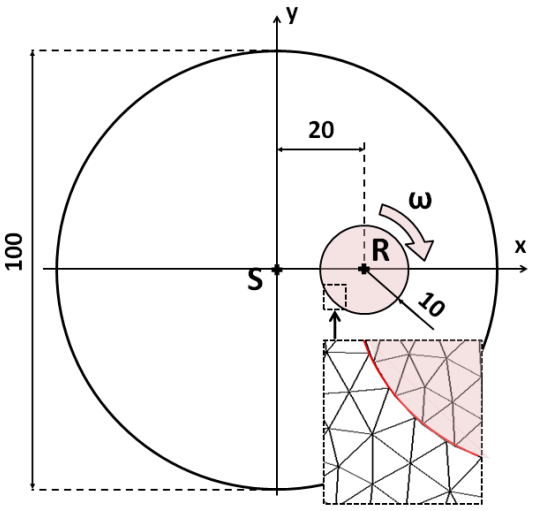

Fig. 6: Computational Domain ($N_c = 4090$)

Boundary condition: At the interface, we test the different MLS-based sliding mesh interfaces methods. At the outer boundaries of the domain, we employ an upwinding technique used by Bernacki et al. [2006] to select only outgoing waves. This kind of absorbing boundary condition is not the purpose of this paper.So, we refer the reader to Khelladi et al. [2011] and Nogueira et al. [2009] for detail information.

2.2 Implementation aspects

MLS parameter setting : To reach 4^{th} order of acuracy, we need a 3^{rd} order reconstruction. Therefore, the shape function derivatives are pushed until 3^{rd} order and then a minimum of $n_{min} = 10$ cells in the stencil surrounding the active cell are used. We add 4 points more ($p = 4$) in the stencil in order to have a numerically stable scheme. Finally $n_t = 14$. The shape parameters of MLS are $k_x = k_y = 5$. This choice is a good compromise of dispersion and dissipation.

Numerical integrations: It is well known that if one wants to preserve the targeted order of accuracy of the finite volume scheme, all the intermediate numerical integrations or differentiations should be estimated at least with the same order of accuracy, see Nogueira et al. [2010]. For these considerations, we used for the present work the following approximations:

– 3^{rd} order Gauss-Legendre quadrature for the integration of the flux (Eqn. (3)).

– 7^{th} order symmetric quadrature of Wandzura and Xiao. [2003] is used for the numerical calculous of μ_{ij} (Eqn. (9)). Shape function derivatives are pushed to the same order as for the extrapolation of flux.

Solver: The pseudo mass-matrix $\mathbb{M}$ is a square matrix of size N_c. Fig. 7 shows the pseudo mass-matrix of the domain shown in Fig. 5 for the half stencil and the full stencil approaches at the interface. Non-zero values appear in blue. The numeration of cells starts from the center of the rotational grid with a distance criterium. Matrix values depend on shape functions and hence $\mathbb{M}$ is a constant matrix for the half stencil at the interface. Moreover, the mass-matrix of the half stencil approach (A) is a block diagonal matrix in which the first block is associated to the rotational grid and the second block is associated to the fixed grid. With the full stencil at the interface, the term μ_{IJ} for the I cells near the interface must be re-computed and the matrix can not be decomposed. The matrix (B) expresses the link between the two grids. In general, the diagonal structure is recovered by enforcing reconstructions that preserves the mean. It is then possible to solve the system with an explicit method. However, it has been proved in the paper by Khelladi et al. [2011] that the maximum order of accuracy reached by this technique is 3. Therefore, in this work, to reach higher order of accuracy, we solve the pseudo mass matrix using an implicit differential algebric solver called IDA, see Hindmarsh et al. [2005]. The time integration method is the variable-order (from 1 to 5), variable-coefficient Backward Differentiation Formula (BDF), with adaptive time-step, described by Li and Petzold [1999] and Brenan et al. [1996]. For the solution to the linear system, Newton/Krylov subspace iterative corrections method based on a scaled preconditioned GMRES solver is used, see Saad and Schultz [1986].

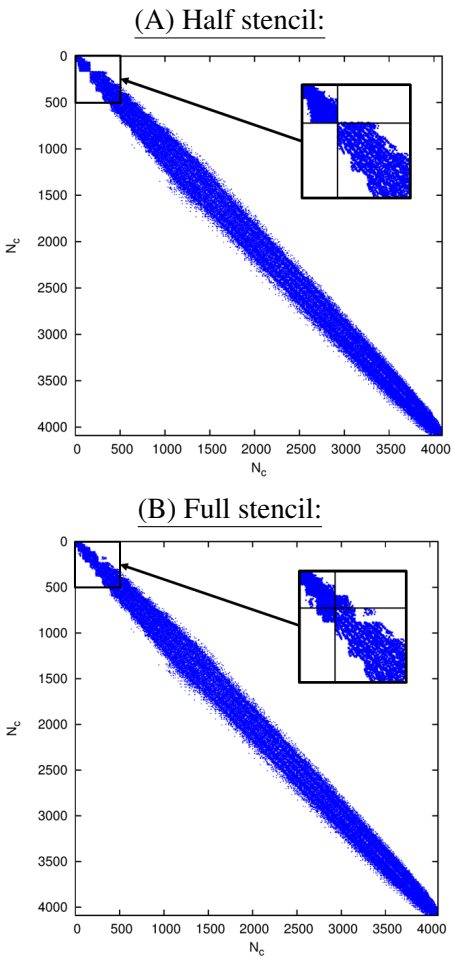

Fig. 7: 4^{th} Order matrix with half (A) and full (B) stencil at the interface. $N_c = 4327$

2.3 Results

The objectives of this section are the validation of MLS-based sliding mesh interfaces 4^{th} space order of accuracy and making a comparison between each of the methods. Numerical convergence of the 4 methods is adressed on different mesh resolutions (N_c from 4090 to 9769) with the quadratic mean errors of the pressure field:

$$L_2(p) = \|\varepsilon_p\|_2 = \left[\frac{1}{A}\sum_{I=1}^{N_c} A_I \varepsilon_{p,I}^2\right]^{1/2} \tag{13}$$

and the maximum error,

$$L_\infty(p) = \|\varepsilon_p\|_\infty = max[|\varepsilon_{p,I}|] \tag{14}$$

where, $\varepsilon_{p,I}$ is the difference between p_I^{ex} (the centroid value of the analytical pressure field) and p_I^{num} (the numerical value).

MLS-based sliding mesh interfaces order of accuracy: Looking at the below Fig. 9, first appearance is that any of the methods used have a very similar order of accuracy. Real orders are lower than the theoretical order. In average, the orders of the maximum error ($\simeq 3$) are lower than the orders of the quadratic mean errors ($\simeq 3.6$). Moreover, the order of the maximum error is very fluctuant. This is due to the use of an unstructured grid. Indeed, the grid distortion tends to reduce the effective order of the method. It's also important to notice that the differences between the full stencil and the half stencil reconstruction is very tiny.

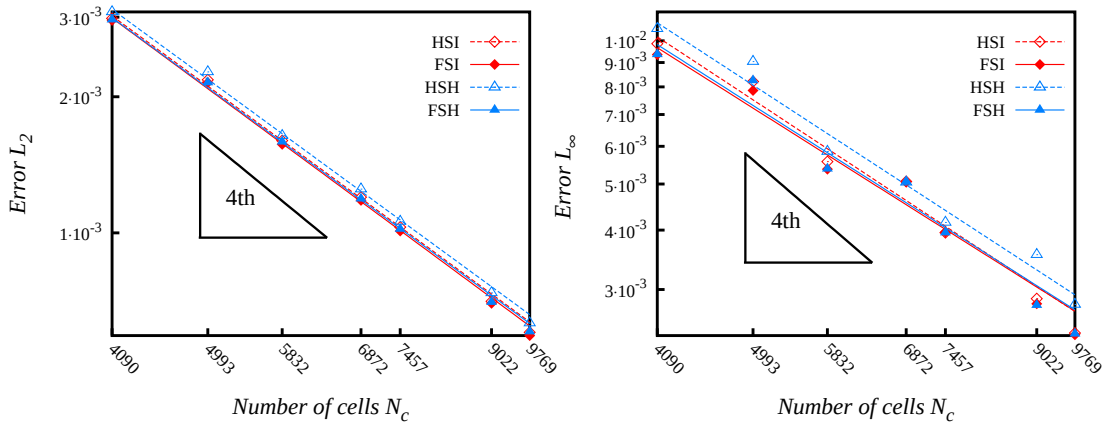

Method		HSI		FSI		HSH		FSH	
Error		$L_2(p)$	$L_\infty(p)$	$L_2(p)$	$L_\infty(p)$	$L_2(p)$	$L_\infty(p)$	$L_2(p)$	$L_\infty(p)$
Grid	4090	2.98E-03	9.86E-03	3.08E-03	1.06E-02	2.95E-03	9.35E-03	2.96E-03	9.36E-03
	4993	2.18E-03	8.21E-03	2.27E-03	9.04E-03	2.15E-03	7.86E-03	2.15E-03	8.25E-03
	5832	1.60E-03	5.57E-03	1.64E-03	5.85E-03	1.57E-03	5.05E-03	1.19E-03	5.05E-03
	6872	1.20E-03	5.06E-03	1.25E-03	5.04E-03	1.18E-03	5.05E-03	1.19E-03	5.05E-03
	7457	1.03E-03	3.95E-03	1.06E-03	4.15E-03	1.01E-03	3.96E-03	1.02E-03	3.95E-03
	9022	7.06E-04	2.87E-03	7.37E-04	3.55E-03	6.99E-04	2.80E-03	7.03E-04	2.78E-03
	9769	6.03E-04	2.43E-03	6.32E-04	2.79E-03	5.93E-04	2.41E-03	6.05E-04	2.42E-03
Slope		**3.58**	**3.05**	**3.60**	**2.93**	**3.57**	**3.05**	**3.58**	**2.95**

Fig. 9: MLS-based Sliding Mesh convergence rate for the pressure solution at $t = 40$ with $\omega = 0,01$

The comparison across computational time of the 4 methods is crucial. Please find the values on the opposite Table (Tab. 1). These results were obtained with a non-optimized sequential solver. An improvement of algorithms should be done. Finally, we see the half stencil halo-cell method as an attractive solution to transfers information from one grid to another. However, please note that using the half stencil with the halo cell approach is not recommended when shock waves are presented in the solution, for example in Euler or Navier Stokes equations, since the conservation errors are not admissible. This is not the case for the full stencil approach. These results will be presented in another work that will be published elsewhere.

Method	Time (s)	Ratio
HSI	253	1
FSI	417	1,6
HSH	234	0,9
FSH	359	1,4

Tab. 1: Time to solve acoustic pulse propagation from t=0 to t=40 ($N_c = 9769, \omega = 0,01$)

Rotational velocity impact As it is shown in Fig. 8 the Halo-cell formulation gives better results than intersection with implicit solver at high rotational velocity. Mention should be made of the speed range of 0 to c_∞ investigated includes most turbomachinery problems. These results are most encouraging but must be analysed more closely. The authors hope provide a significant study of non dimensional rotational velocity impact.

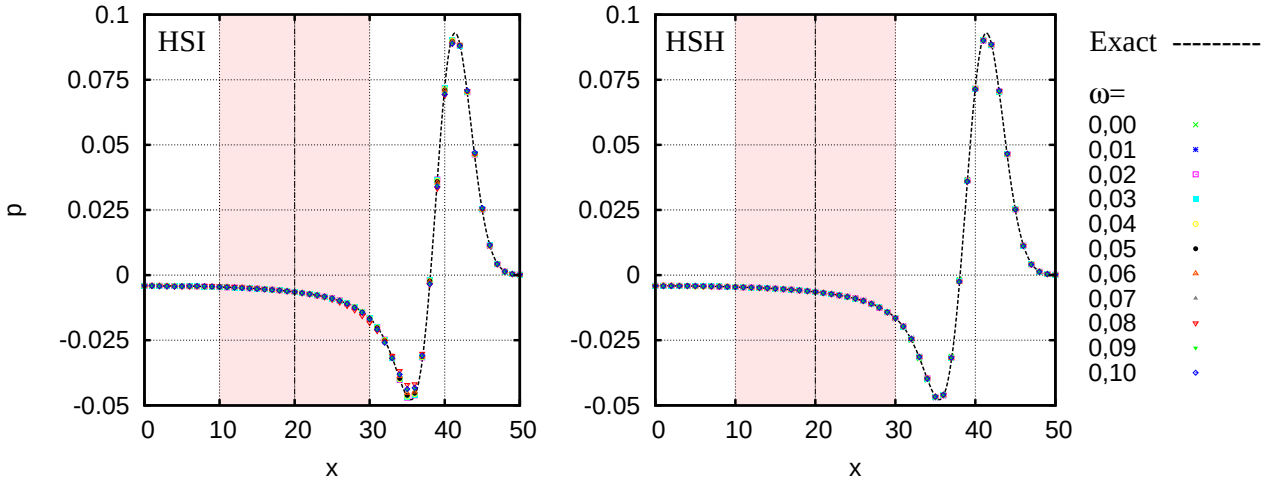

Fig. 8: Section of the pressure solution along (S, $\overrightarrow{x}$) at $t = 40$, $N_c = 9769$, 4^{th} space order. Comparison between the Intersection approach (left) and the Halo-cell (right) approach for different rotational velocity. The pink area corresponds to the moving grid zone.

2.3 Numerical exemple: Monopole's radiation in a shear mean flow

The vector $\mathbf{H}$ represents complex refraction effects in the propagation field which is crucial in turbomachinery noise problem. With a mean flow non-uniformly convected, the inhomogeneous term $\mathbf{H}$ from the LEE is not equal to zero. It is important to notice that, as it has been shown by C. Prax and Nadal [2007], this term can lead to numerical instabilities. To illustrate the refraction effect and the stability of the method qualitatively, a symmetric horizontally sheared flow, similar to those used by C. Bogey and Juvé [2002] and Cand [2005] is given as input $U_0 = [1, u_s, 0, 1/\gamma]$ with:

$$u_s = M_s tanh(y/2) \tag{15}$$

where the maximum Mach number M_s is 0.125. A monopole source is implemented by using the vector S in Eqn. 1), which yields:

$$\boldsymbol{S}(x, y, t) = \epsilon \cdot \mathrm{e}^{-\alpha r} sin(\omega_m t) \times [1\ 0\ 0\ 1]^T \tag{16}$$

where $r = [(x - x_s)^2 + (y - y_s)^2]^{1/2}$ is the radial distance to the domain's center. The angular frequency is $\omega_m = 2\pi/30$, the amplitude is taken as $\epsilon = 0.5$ and $\alpha = ln2/2$. All the variables are made dimensionless with the same reference scales than the acoustic benchmark. The computation is performed with two non-conform interfaces as it is described in Fig. 9-A). Please find Fig. B) the result of the sheared mean flow case.

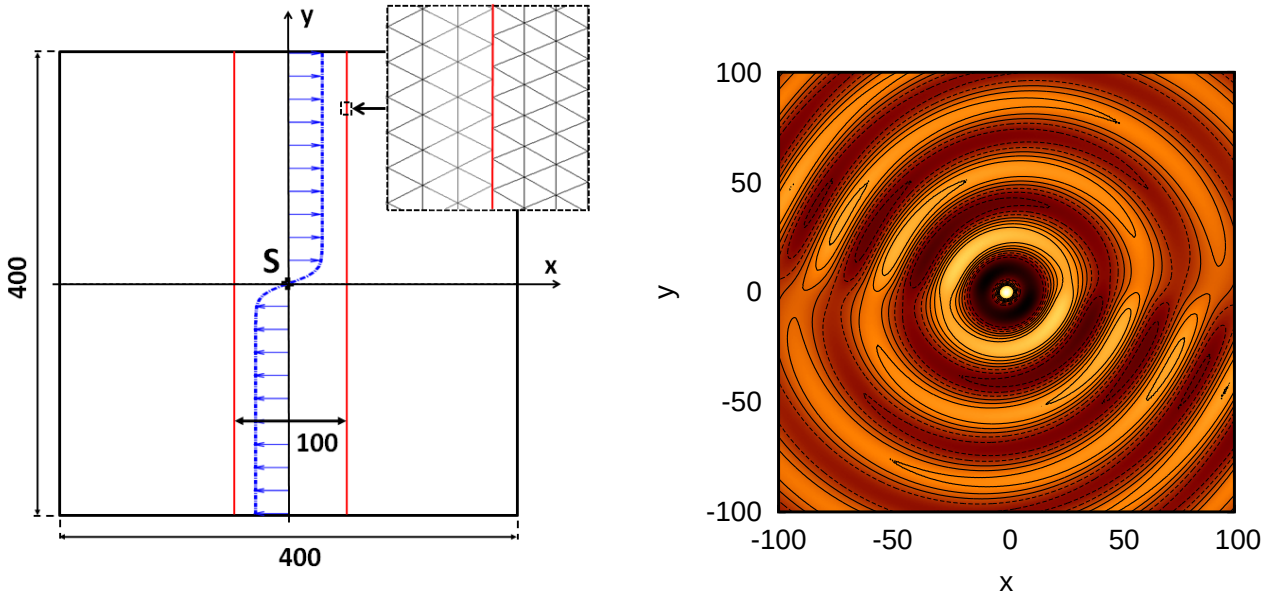

Fig. 9: A) Computational Domain : Two interfaces with non-conform cell ($N_c = 160138$) B) Monopole's radiation in a shear mean flow ($M_s = 0.125$) at adimensional time t=190 (4th space order, HSH). Pressure isocontours: $0, \pm 210^2, \pm 410^2, \pm 610^2$. Negative isocontours are in dotted lines.

CONCLUSIONS

Two families of high-order MLS-based sliding mesh interfaces were successfully used to solve a CAA benchmark on unstructured grids. At the moment, only implicit time solver was tested with the sliding mesh mass-matrix based FV-MLS. A convergence study was performed for each approach. The study reveals that both the halo cell method and the intersection method can reach high accuracy. A first evaluation of the impact of rotational velocity on results has been done. The accuracy and robustness of the new methodology has been shown with a sheared mean flow. No instability has been observed. Also, it would be interesting to investigate more deeply the impact on results of mesh anisotropy. Finally, our future objective is to use an explicit solver well fitted for CAA. To achieve this, we need to inverse the pseudo mass-matrix or use lumping techniques. We hope to succeed in these points before the conference.

ACKNOWLEDGEMENTS

The authors would like to express their gratitude to Pr. Farid Bakir, Dr. Jean Camille Chassaing and Mr. Ewen Marechal for the exchanges during the writing of the paper. The autors would also like to acknowledge the financial support for the PhD thesis garanted by Snecma, part of Safran group and Valeo.

References

M. Bernacki, S. Lanteri, and S. Piperno. Time-domain parallel simulation of heterogeneous wave propagation on unstructured grids using explicit, non-diffusive, discontinuous Galerkin methods. *J. Computational Acoustics*, 14(1):57–82, 2006.

C. Bogey and C. Bailly. Three dimensional non reflective boundary conditions for acoustic simulations: far field formulation and validation test cases. *ACTA ACUSTICA UNITED WITH ACUSTICA Vol. 88, 463-471 2002*, 2002.

K.E. Brenan, S.L. Campbell, and L.R. Petzold. Numerical solution of initial-value problems in differential-algebraic equations. *SIAM Philadelphia, Pa*, 1996.

C. Bailly C. Bogey and D. Juvé. Computation of flow noise using source terms in linearized euler's equations. *AIAA JOURNAL Vol. 40, No. 2, February 2002*, 2002.

F. Golanski C. Prax and L. Nadal. Control of the vorticity mode in the linearized euler equations for hybrid aeroacoustic prediction. *Journal of Computational and Physics, volume 227, Pages 6044-6057*, 2007.

M. Morgan Cand. A 3d high-order aeroacoustics model for turbomachinery fan noise propagation. *PhD thesis, Imperial College London, Department of Mechanical Engineering, London, England, June 2005*, 2005.

L. Cueto-Felgueroso, I. Colominas, J. Fe, F. Navarrina, and M. Casteleiro. High-order finite volume schemes on unstructured grids using moving least squares reconstruction. application to shallow water dynamics. *Int. J. Numer. Meth. Engng*, 2006.

L. Cueto-Felgueroso, I. Colominas, X. Nogueira, F. Navarrina, and M. Casteleiro. Finite volume solvers and moving least-squares approximations for the compressible Navier-Stokes equations on unstructured grids. *Computer Methods in Applied Mechanics and Engineering*, 196:4712–4736, 2007.

E. Ferrer and R.H.J. Willden. A high order discontinuous galerkin fourier incompressible 3d navier-stokes solver with rotating sliding meshes. *Journal of Computational Physics*, 231:7037–7056, 2012.

A.C. Hindmarsh, P.N. Brown, K.E. Grant, S.L. Lee, R. Serban, D.E. Shumaker, and C.S. Woodward. Sundials: Suite of nonlinear and differential/algebraic equation solvers. *ACM Transactions on Mathematical Software*, 31(3):363–396, 2005.

S. Khelladi, X. Nogueira, F. Bakir, and I. Colominas. Toward a higher-order unsteady finite volume solver based on reproducing kernel particle method. *Computer Methods in Applied Mechanics and Engineering*, 200:2348–2362, 2011.

S. Li and L. R. Petzold. Design of new daspk for sensitivity analysis. *Technical Report of Computer Science Department (TRCS99-23), University of California, Santa Barbara*, 1999.

G. R. Liu. *Mesh free methods: moving beyond the finite element method.* CRC Press, Boca Raton, 2003.

W. K Liu, W. Hao, Y. Chen, S. Jun, and J. Gosz. Multi-resolution reproducing kernel particle methods. *Computational Mechanics*, 20:295–309, 1997.

X. Nogueira, L. Cueto-Felgueroso, I. Colominas, S. Khelladi, F. Navarrina, and M. Casteleiro. Resolution of computational aeroacoustics problem on unstructured grids with high-order finite volume scheme. *Journal of Computational and Applied Mathematics, doi:10.1016/j.cam.2009.08.067*, 2009.

X. Nogueira, I. Colominas, L. Cueto-Felgueroso, and S. Khelladi. On the simulation of wave propagation with a higher-order finite volume scheme based on reproducing kernel methods. *Computer Methods in Applied Mechanics and Engineering, Volume 199, Issues 2324, 15 April 2010, Pages 1471-1490*, 2010.

P.L. Roe. Approximate Riemann solvers, parameter vectors, and difference schemes. *J. Comput. Phys., 43:357-372*, 1981.

Y. Saad and M.H. Schultz. Gmres: A generalized minimal residual algorithm for solving non-symmetric linear systems. *SIAM J. Sci. Stat. Comp.*, 7:856–869, 1986.

C.K.W. Tam and J.C. Webb. Dispersion-relation-preserving finite difference schemes for computational aeroacoustics. *J. Comput. Phys.*, 107:262–281, 1993.

JY. Trepanier, M. Reggio, H. Zhang, and R. Camarero. A finite-volume method for the euler equations on arbitrary lagrangian-eulerian grids. *Computers Fluids Vol. 20, No. 4, pp. 399-409, 1991*, 1991.

S. Wandzura and H. Xiao. Symmetric quadrature rules on a triangle. *Computers and Mathematics with Applications, 45:1829 -1840, 2003*, 2003.